electronics

MDPI

Article

An Improved Current Signal Extraction-Based High-Frequency Pulsating Square-Wave Voltage Injection Method for Interior Permanent-Magnet Synchronous Motor Position-Sensorless Control

Dongyi Meng [1,2], Qiya Wu [1,2], Jia Zhang [1,2] and Lijun Diao [1,2,*]

[1] School of Electrical Engineering, Beijing Jiaotong University, Beijing 100044, China; dymeng@bjtu.edu.cn (D.M.)
[2] Key Laboratory of Vehicular Multi-Energy Drive Systems (VMEDS), Ministry of Education, Beijing Jiaotong University, Beijing 100044, China
* Correspondence: ljdiao@bjtu.edu.cn

Abstract: The high-frequency (HF) voltage injection method is widely applied in achieving position-sensorless control for interior permanent-magnet synchronous motors (IPMSMs). This method necessitates precise and rapid extraction of the current signal for accurate position estimation and field-oriented control (FOC). In the traditional methods, the position error signal and fundamental current are extracted from the current signal using band-pass filters (BPFs) and low-pass filters (LPFs), or a method based on time-delay filters. However, the traditional extraction method falls short in ensuring simultaneous dynamic performance and accuracy, particularly when the switching frequency is limited or when encountering harmonic and noise interference. In this article, a novel HF pulsating square-wave voltage injection method based on an improved current signal-extraction strategy is proposed to improve the extraction accuracy while maintaining good dynamic performance. The newly devised current signal-extraction method is crafted upon a notch filter (NF). Through harnessing NF's effective separation characteristics of specific frequency signals, the current signal is meticulously processed. This process yields the extraction of the position error signal and fundamental-current component, crucial for accurate position estimation and motor FOC. Simulation and hardware-in-the-loop (HIL) testing are conducted to validate the effectiveness of the proposed approach.

Keywords: IPMSM; position-sensorless control; HF voltage injection; signal extraction

Citation: Meng, D.; Wu, Q.; Zhang, J.; Diao, L. An Improved Current Signal Extraction-Based High-Frequency Pulsating Square-Wave Voltage Injection Method for Interior Permanent-Magnet Synchronous Motor Position-Sensorless Control. *Electronics* **2024**, *13*, 2227. https://doi.org/10.3390/electronics13112227

Academic Editors: Ahmed Abu-Siada and Pedro J. Villegas

Received: 5 March 2024
Revised: 22 May 2024
Accepted: 29 May 2024
Published: 6 June 2024

1. Introduction

In the past decades, IPMSMs have found application in various industries and traction-drive systems due to their high efficiency, compact size, precise control, elevated power density and the extensive operating speed range [1–3]. Field-oriented control (FOC) stands as a cornerstone of high-performance control strategies for Interior Permanent-Magnet Synchronous Motors (IPMSMs), offering precise regulation of the motor's magnetic flux and torque. Traditionally, the implementation of FOC necessitated the use of position sensors to accurately ascertain rotor position and speed, ensuring optimal motor performance. However, in recent decades, considerable attention has shifted towards sensorless control methods for IPMSMs.

The emergence of sensorless control techniques represents a significant advancement, eliminating the reliance on physical position sensors and offering a host of benefits. These benefits include cost reduction through the elimination of sensor procurement and installation, simplified system design by removing additional hardware components, increased system reliability due to reduced points of failure, and improved efficiency through advanced signal-processing algorithms and motor model estimations. Additionally, sensorless

control methods afford greater flexibility and adaptability, enabling seamless integration into existing systems without requiring extensive modifications. The growing interest in sensorless control of IPMSMs underscores a broader trend towards enhancing motor control efficiency, reliability, and performance while reducing overall system complexity and cost [4]. As sensorless control techniques continue to evolve and mature, they are poised to play a pivotal role in driving the widespread adoption of IPMSMs across diverse industrial applications and traction-drive systems.

In position-sensorless control applications, accurate position estimation is essential for ensuring stable motor operation, precise speed control, and efficient torque generation [5]. It enables the motor controller to maintain optimal performance even under varying operating conditions and load disturbances. Moreover, accurate position estimation enhances the motor's fault tolerance in sensorless control applications, allowing the system to detect and respond to faults effectively without relying on sensor feedback. Furthermore, in the realm of railway-traction applications, low switching frequencies are typically employed. PMSM sensorless control is currently being explored in this context [6]. Additionally, in the event of speed sensor failures, sensorless control can serve as a redundant backup, enhancing fault tolerance in the case of position-sensor malfunction.

The sensorless control strategies for IPMSMs can be classified into two main groups [7]: model-based methods designed for medium-to-high speed operating ranges, and saliency-based methods intended for low-speed operational ranges. The model-based method for sensorless control of IPMSMs focuses on estimating the rotor position and speed by observing the motor's back-electromotive force (EMF) [8] or flux linkage [9]. This approach typically involves the use of a position observer, which utilizes mathematical models of the motor's dynamics and electromagnetic properties to estimate the rotor position and speed. Several techniques fall under the umbrella of model-based sensorless control methods, including the sliding mode observer, the extended Kalman filter, the MRAS observer [10–13], etc. The model-based methods leverage the inherent relationship between the motor's electrical quantities (such as back EMF or flux linkage) and its mechanical parameters (such as rotor position and speed) to estimate the rotor state without the need for physical sensors. By utilizing mathematical models and advanced estimation techniques, model-based sensorless control methods offer robust and accurate rotor position and speed estimation, enabling efficient and reliable control of IPMSMs in various applications. These model-based methods have exceptional performance in medium-to-high-speed areas; however, they encounter challenges in the low-speed region because of the diminished signal-to-noise ratio (SNR) resulting from factors such as harmonics and inverter nonlinearity [14]. To extend sensorless control in the low-to-zero-speed region, researchers have devised the saliency tracking methods, and the HF voltage injection-based method represents a notable category of methods. Based on the injection reference frame of the injection signal, HF voltage injection methods can be broadly classified into rotating voltage injection methods [15–20] and pulsating voltage injection methods [21–24]. Depending on the injection signal, the pulsating voltage injection methods can be further subdivided into pulsating sinusoidal voltage injection (PSVI) and pulsating square-wave voltage injection (PSWVI) methods. By leveraging the distinctive characteristics of HF voltage signals and analyzing the motor's response, these methods provide robust and accurate rotor position and speed estimation, enabling effective control of IPMSMs across a wide range of operating conditions.

In the realm of sensorless control for IPMSMs, the application of HF signal injection methods presents a promising avenue for accurately estimating rotor speed and position, particularly in low-to-zero-speed regions. However, the accuracy of these estimations hinges on several interconnected factors that must be carefully considered and optimized, including the choice of the injection signal, the processing and extraction of the position error signal, and design of the position observer [25,26]. In the traditional HF voltage injection methods, the HF induced current and the fundamental current are extracted by using a band-pass filter (BPF) and a low-pass filter (LPF). Nonetheless, employing the

BPF + LPF-based strategy for signal extraction can degrade the dynamic performance of the system [27,28]. In order to enhance the dynamic performance of the sensorless algorithm, [29] proposed a signal processing method without LPF, in which the position error signal is obtained directly through arithmetic calculations, bypassing the need for low-pass filters, which not only eliminates time delays but also enhances the system's dynamic performance. But the BPF is still needed when extracting the HF induced-current signal, so the bandwidth of the system is still limited. In [30,31], a method is proposed for directly calculating the estimated rotor position through the utilization of the arctangent function. This method can improve the dynamic performance of the system; however, it needs the frame of the HF injected voltage to be changed, which will complicate the signal demodulation process and elevate the challenge in parameter design. To eliminate both the BPF and LPF and extend the bandwidth of the position estimation loop, [32] proposed a time-delay filter-based signal-extraction method building upon the symmetric characteristic of the injected voltage signal. This method eliminates the BPF and LPF at the same time, and has a higher bandwidth compared with the traditional methods. However, in the application of this method, the fundamental current is assumed to remain constant between the two sampling instants. Nevertheless, in specific applications like high-power railway-traction systems, the switching frequency is limited to several hundred hertz, strategically reducing switching losses and optimizing inverter efficiency [13,31]. This can lead to substantial errors, as a low switching frequency may cause significant variations in fundamental-current values between two sampling moments. Furthermore, in signal separation, aside from employing sampling bandpass filters (BPFs), notch filters are also commonly utilized. Through proper design, notch filters can be employed for both filtering and separating signals [33]. In [34], the master-slave adaptive notch filter (NF) is employed to effectively filter and process the observed back-electromotive force (EMF). This approach offers robust filtering capabilities, particularly suitable for use with sliding-mode position observers. Similarly, [35] presents a novel least mean squares (LMS)-based adaptive NF designed specifically for harmonic suppression. While both methods demonstrate efficacy in enhancing signal quality for high-speed region applications, their direct application in HF signal injection methods necessitates careful reconsideration and redesign to ensure compatibility and optimal performance. Therefore, further research and adaptation may be required to adapt these techniques for signal injection purposes.

To address the aforementioned issues, this paper proposes a novel HF PSWVI method based on an improved current signal-extraction strategy. The improved strategy proposed for current signal extraction relies on the implementation of the notch filter (NF). It is designed to extract the position error signal and fundamental-current component, ensuring accurate position estimation and FOC. This approach not only eliminates the need for the BPF and LPF, thereby extending the bandwidth, but also safeguards the estimation results from being impacted by harmonics and noise and can overcome the challenges associated with low switching frequency. The subsequent sections of this article are structured as follows: Section 2 outlines the HF mathematical model of IPMSM and the mechanism of the conventional PSWVI. In Section 3, the characteristics of the notch filter are analyzed, and the proposed HF PSWVI method is introduced. In Section 4, simulation and hardware-in-the-loop (HIL) testing is carried out, the results of the conventional and the proposed HF PSWVI methods are compared, and the validation of the effectiveness of the suggested control strategy is confirmed. Ultimately, the findings are summarized in Section 5.

2. Analysis of HF Pulsating Square-Wave Voltage Injection Methods

2.1. Mathematical Principle of HF PSWVI

The voltage model of the IPMSM in the rotor dq-reference frame can be represented as follows:

$$\begin{bmatrix} u_d \\ u_q \end{bmatrix} = \begin{bmatrix} pL_d + R_s & -\omega_e L_q \\ \omega_e L_d & pL_q + R_s \end{bmatrix} \begin{bmatrix} i_d \\ i_q \end{bmatrix} + \begin{bmatrix} 0 \\ \omega_e \psi_f \end{bmatrix} \quad (1)$$

where u_d, u_q and i_d, i_q are current and voltage in the dq-reference frame respectively, L_d and L_q represent the dq axis inductances, ψ_f denotes the flux linkage of the permanent magnet, ω_r denotes the rotor speed, and p represents the differential operator.

Owing to the significantly higher frequency of the injected signal compared to the fundamental operating frequency, the contributions of the stator-resistance voltage drop, rotating voltage, and back EMF in Equation (1) can be disregarded. The high-frequency injected voltage can indeed induce increased eddy currents, resulting in an increase in the motor's equivalent resistance. However, since the injected voltage used in this paper operates at 500 Hz, with an overall moderate injection frequency, the eddy currents generated are minimal. Under high-frequency signal excitation, the IPMSM can be approximately treated as an inductive load. Hence, the HF mathematical model of the IPMSM can be represented as

$$\begin{bmatrix} u_{dh} \\ u_{qh} \end{bmatrix} = \begin{bmatrix} pL_d & 0 \\ 0 & pL_q \end{bmatrix} \begin{bmatrix} i_{dh} \\ i_{qh} \end{bmatrix} \tag{2}$$

The subscript h represents the HF component.

Figure 1 shows the coordinate reference frames of the IPMSM; the dq coordinate axis denotes the real rotor reference frame (RRRF), the $\hat{d}\hat{q}$ coordinate axis represents the estimated rotor reference frame (ERRF), and $\Delta\theta$ denotes the angle error between the RRRF and ERRF. In theory, high-frequency voltage signals can be injected into both the d-axis and q-axis. However, to mitigate the influence of the injected current on the motor torque, the paper specifically chooses to apply voltage injection along the d-axis. The HF square-wave voltage signal is injected in the ERRF, as in the following expression

$$u_{inj} = \begin{bmatrix} u_{\hat{d}inj} \\ u_{\hat{q}inj} \end{bmatrix} = \begin{bmatrix} (-1)^n U_h \\ 0 \end{bmatrix} \tag{3}$$

where $u_{\hat{d}inj}$ and $u_{\hat{q}inj}$ represent the HF voltage components in the $\hat{d}\hat{q}$ axis of ERRF, U_h denotes the amplitude of the injection signal, and n represents the index of the control period.

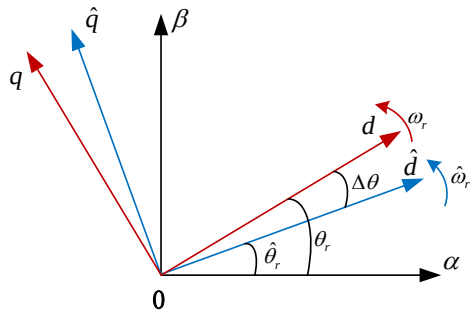

Figure 1. Coordinate reference frames of IPMSM.

The conversion of the injection HF-voltage components from the ERRF to the RRRF can be articulated as follows:

$$\begin{bmatrix} u_{dh} \\ u_{qh} \end{bmatrix} = \begin{bmatrix} cos\Delta\theta & sin\Delta\theta \\ -sin\Delta\theta & cos\Delta\theta \end{bmatrix} \begin{bmatrix} u_{\hat{d}inj} \\ u_{\hat{q}inj} \end{bmatrix} \tag{4}$$

The relationship between HF induced currents in the dq synchronous rotating coordinate and the α-β stationary coordinate system can be formulated as the following:

$$\begin{bmatrix} i_{\alpha h} \\ i_{\beta h} \end{bmatrix} = \begin{bmatrix} cos\theta_r & -sin\theta_r \\ sin\theta_r & cos\theta_r \end{bmatrix} \begin{bmatrix} i_{dh} \\ i_{qh} \end{bmatrix} \tag{5}$$

Upon substituting Equation (4) into (2), the HF induced currents in the dq-axis can be obtained. Further transforming it into the α-β stationary reference frame according to (5), the expression for the HF induced currents in α-β-axis can be derived as

$$\begin{bmatrix} pi_{\alpha h} \\ pi_{\beta h} \end{bmatrix} = \frac{u_{\hat{d}inj}}{\omega_h L_{dh} L_{qh}} \begin{bmatrix} L_{\sum} cos\hat{\theta}_r - \Delta L cos(\theta_r + \Delta\theta) \\ L_{\sum} sin\hat{\theta}_r - \Delta L sin(\theta_r + \Delta\theta) \end{bmatrix} \tag{6}$$

where $L_{\sum} = \frac{L_d + L_q}{2}, \Delta L = \frac{L_d - L_q}{2}$.

It is evident that the HF induced currents encompass positional information, offering the potential for estimating the rotor speed and position of the IPMSM.

2.2. Analysis of the Conventional Signal-Extraction Methods

When employing an HF PSWVI method in the d-axis of the ERRF, the motor currents comprise both HF induced-current components and fundamental components, which can be utilized to extract the position error signal and fundamental-current component for the rotor position observation and motor FOC.

The BPF+LPF-based method is a conventional approach to extract the position error signal and the fundamental-current components from the rotor currents. Figure 2 illustrates the signal-extraction process. The extraction of the HF induced-current component is achieved through the utilization of the BPF, and the fundamental component is obtained by applying the LPF.

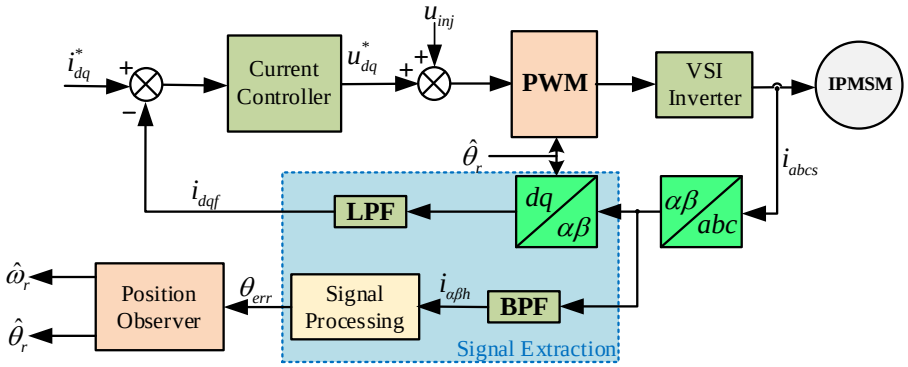

Figure 2. PSWVI method with BPF + LPF.

The time-delay filter signal-extraction (TDFSE) method is another conventional signal-extraction strategy [32,36]; Figure 3 depicts its signal-extraction process.

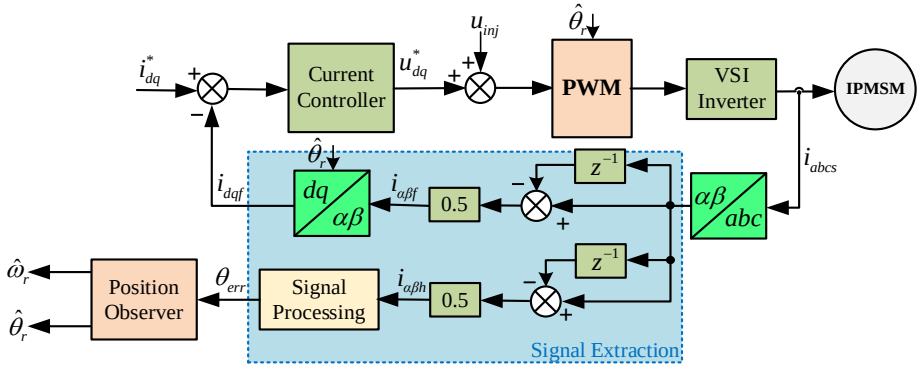

Figure 3. PSWVI method with TDFSE strategy.

In this method, the fundamental current is assumed to remain constant in the adjacent sampling periods. Due to the symmetry inherent in the injected square-wave voltage, the induced currents maintain a consistent magnitude but exhibit opposite polarities in two

successive sampling periods. The extraction of the fundamental-current component and the HF induced current can be accomplished as follows

$$\begin{cases} i_f(n) = \frac{i_s(n)+i_s(n-1)}{2} \\ i_h(n) = \frac{i_s(n)-i_s(n-1)}{2} \end{cases} \tag{7}$$

where the subscript f denotes the fundamental-current component, while h represents the HF induced-current component.

Hence, the discrete-time representation of this filter can be articulated as

$$\begin{cases} G_f(z) = \frac{1+z^{-1}}{2} \\ G_h(z) = \frac{1-z^{-1}}{2} \end{cases} \tag{8}$$

Compared with the BPF + LPF-based method, the TDFSE strategy has a higher bandwidth and a better dynamic performance and it has attained heightened ubiquity in HF PSWVI application. However, in some low switching-frequency applications, the fundamental-current component undergoes substantial variations between two successive sampling moments, making it inappropriate to assume its constancy. Additionally, in practical applications, sampled currents often contain harmonics and noise, and the motor current can be represented by the following expression:

$$i_s = i_f + i_h + i_{hn} \tag{9}$$

where i_{sf} and i_{sh} denote the fundamental- and the HF induced-current component, and i_{hn} represents the harmonics and the noise current.

The presence of harmonics and the noise current will also adversely impact the accuracy of current extraction, consequently influencing the observation of the motor rotor and its position.

3. Proposed HF PSWVI Method Based on Improved Signal-Extraction Strategy

When employing the HF PSWVI method, to ensure accurate observation of rotor speed and position while maintaining optimal dynamic performance, this article introduces a novel signal-extraction approach based on NF. The precision and dynamic performance of the control system's extraction have been significantly improved.

3.1. Review of NF Characteristics

In this section, the characteristic of the NF is delved into, as it plays a crucial role in the context of current-signal extraction. The NF presents a distinct advantage over a normal band-stop filter by providing a more precise and selective attenuation of a specific frequency, allowing for effective elimination of interference without affecting neighboring frequencies so extensively [37,38]. The transfer function of the standard NF can be rewritten as

$$G_{NF}(s) = \frac{s^2 + \omega_0^2}{s^2 + \omega_c s + \omega_0^2} \tag{10}$$

where ω_0 signifies the central rejected frequency, while ω_c denotes the width of the rejected band.

Defining $\omega_0 = 2\pi f_0, \omega_c = 2\pi f_c$, Figure 4 depicts the bode plots for the NF with the central rejected frequency $f_0 = 500$ Hz, and three widths of the rejected bands are selected, where f_c = 1, 10 and 20 Hz. When the input signal frequency closely approaches ω_0, the gain in the NF is very small, and as ω_c increases, the frequency selection capacity diminishes. With reasonable settings, the NF is very suitable for extracting and separating specific signals.

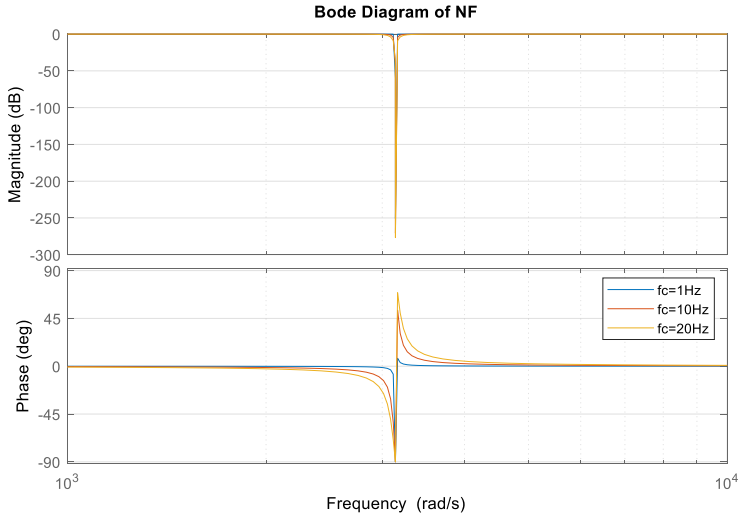

Figure 4. Bode plot of NF.

3.2. HF PSWVI Strategy Based on Improved Signal-Extraction Method

The diagram in Figure 5 outlines the key blocks involved in the NF-based improved position-error signal-extraction method. According to Formula (9), the sampling currents in the $\alpha\beta$ stationary coordinate system can be represented as

$$\begin{cases} i_{\alpha s} = i_{\alpha f} + i_{\alpha h} + i_{\alpha hn} \\ i_{\beta s} = i_{\beta f} + i_{\beta h} + i_{\beta hn} \end{cases} \tag{11}$$

where the subscripts *f*, *h* and *hn* denote the fundamental current, the HF induced current, and the harmonics and the noise current, respectively.

Similarly, the sampling currents in the *dq* rotor reference-frame system can be represented as

$$\begin{cases} i_{ds} = i_{df} + i_{dh} + i_{dhn} \\ i_{ds} = i_{df} + i_{dh} + i_{dhn} \end{cases} \tag{12}$$

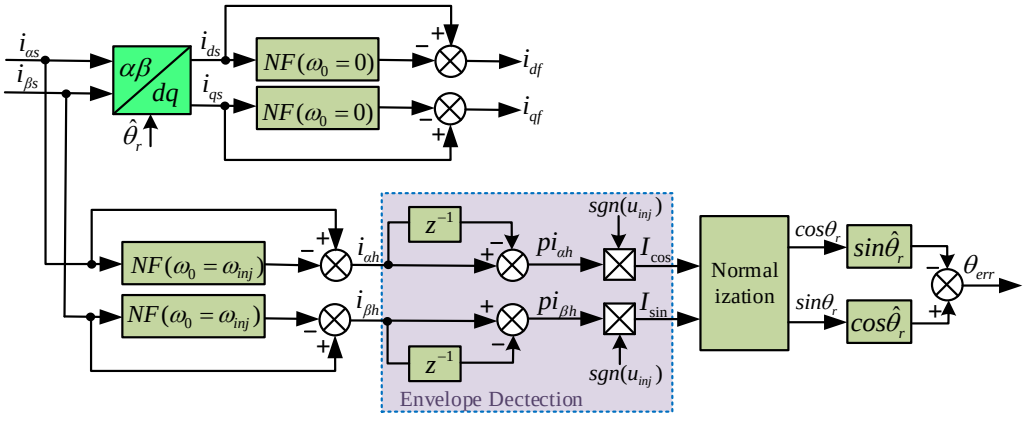

Figure 5. Block diagram of improved NF-based signal-extraction (NFSE) method.

In the process of current demodulation, a NF configured with a center frequency aligned with the frequency of the injection voltage signal is employed to separate the HF induced-current signal from the sampled current. Formula (13) illustrates the result after the input current signal passes through the NF.

$$NF\left(i_{\alpha\beta s}\right) = NF(i_{\alpha\beta f} + i_{\alpha\beta h} + i_{\alpha\beta hn}) \simeq i_{\alpha\beta f} + i_{\alpha\beta hn} \tag{13}$$

By subtracting the NF filtered signal from the original signal, the HF induced-current signal is acquired and the harmonics and noise components are filtered out.

Furthermore, to accomplish vector control, it is essential to extract the fundamental current in the dq rotor reference frame; similar to the process of separating HF induced currents, an NF is employed with the center frequency set to 0 Hz. When ω_0 is set to zero, when A is set to 0, Equation (10) can be written as Equation (14), and in this scenario, the NF effectively functions as a high-pass filter.

$$G'_{NF}(s) = \frac{s}{s + \omega_c} \tag{14}$$

Upon convergence, the estimated position aligns with the actual position, $\Delta\theta \approx 0$, $\hat{\theta}_r \simeq \theta_r$, according to Formula (6); the expression for the envelope curves of the HF induced currents is as follows:

$$\begin{cases} I_{\cos} = K \cdot cos\theta_r \\ I_{\sin} = K \cdot sin\theta_r \end{cases} \tag{15}$$

where $K = U_h/(\omega_h L_d)$, and ω_h denotes the frequency of the injected square-wave voltage.

After the HF induced currents are separated, the envelope curves can be detected by the envelope detector in Figure 5 [32]. The envelope curves of the HF induced currents contain position information, which can be utilized for extracting the rotor speed and position of the IPMSM. In theory, the estimated rotor position and angle can be directly calculated using Equation (15). However, due to the instantaneous nature of the calculation, even when the estimated results are filtered, significant fluctuations may occur. To achieve smoother and more accurate estimation results, a position observer is employed after extracting the envelope of the HF induced current to estimate the rotor position and speed of the motor.

In order to eliminate the coefficient K in Equation (15), the extracted envelope is normalized. Subsequently, the position error signal can be derived as the following:

$$\theta_{err} \approx \sin(\theta_r - \hat{\theta}_r) = \sin\theta_r \cos\hat{\theta}_r - \cos\theta_r \sin\hat{\theta}_r \tag{16}$$

Figure 6 illustrates the control structure of the HF PSWVI strategy with the proposed improved position-error signal-extraction method. Following the extraction of the position error signal, a position observer is implemented to estimate the rotor position and speed of the IPMSM. A PI-form position observer introduced in [29] is applied in this article.

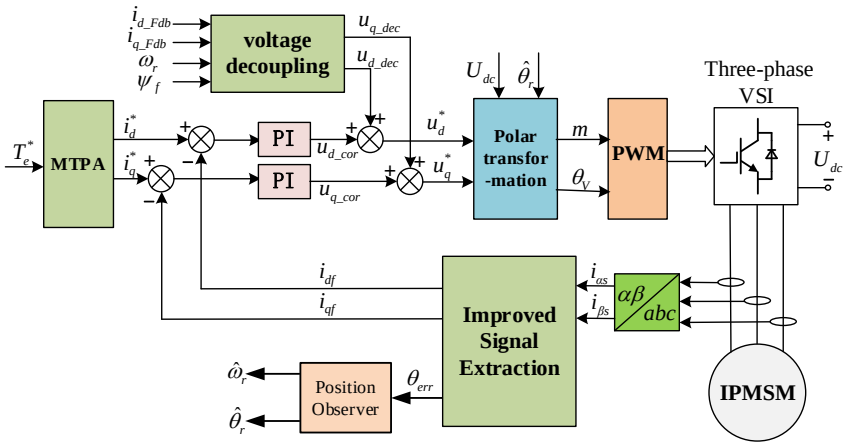

Figure 6. Block Diagram of HF PSWVI strategy with improved signal-extraction method.

4. Simulation and Experimental Validations

4.1. Simulation Analysis

To validate the viability of the proposed algorithm, the benchmark IPMSM drive system as outlined in Table 1 is applied in the simulation testing with the MATLAB/Simulink 2022b.

The simulation details include a "discrete" solver type with a step size of 1×10^{-6} s. The IPMSM and inverter are modeled using Simscape library components. The controller sampling-time and control period are established at 10 kHz. Additionally, the converter switching frequency is configured at 500 Hz, employing SVPWM modulation to accurately simulate the real applications in the traction-drive system. During the simulation testing, the proposed HF PSWVI strategy with the improved signal-extraction method illustrated in Figure 6 is employed, where the IPMSM drive control is based on vector control. The injection frequency is set to match the switching frequency at 500 Hz, while the injection voltage amplitude is configured at 30 V. More specific control parameters are provided in Table 2.

Table 1. Parameters of the IPMSM.

Parameters	Values	Parameters	Values
DC link voltage	900 V	No. of pole pairs p	4
Rated power	300 kW	Stator resistance	0.0066254 Ω
Rated frequency	200 Hz	*d*-axis inductance	0.3062 mH
Rated current	533 A (RMS)	*q*-axis inductance	0.498 mH
Peak current	696 A (RMS)	Flux linkage	0.128046 Wb

Table 2. Parameters of controllers and filters.

Parameter Items	Parameter Values
PI for the stator current	$K_i = 0.12, K_p = 10$
Notch filter	$\omega_0 = 2\pi f_0, \omega_c = 2\pi f_c$, $f_0 = 500$ Hz, $f = 0.1$ Hz
PI for the position observer	$K_i = 32, K_p = 40$

To analyze the steady-state characteristics of the proposed approach, we assume that the motor is subjected to a mechanical load with substantial inertia and operates at a constant speed, and that the torque command is configured to be 1000 N.m at steady state. The results depicted in Figures 7 and 8 represent the outcomes of steady-state performance simulation testing for the conventional TDFSE method and the proposed NFSE method, respectively, at the speeds of 20 Hz and 10 Hz.

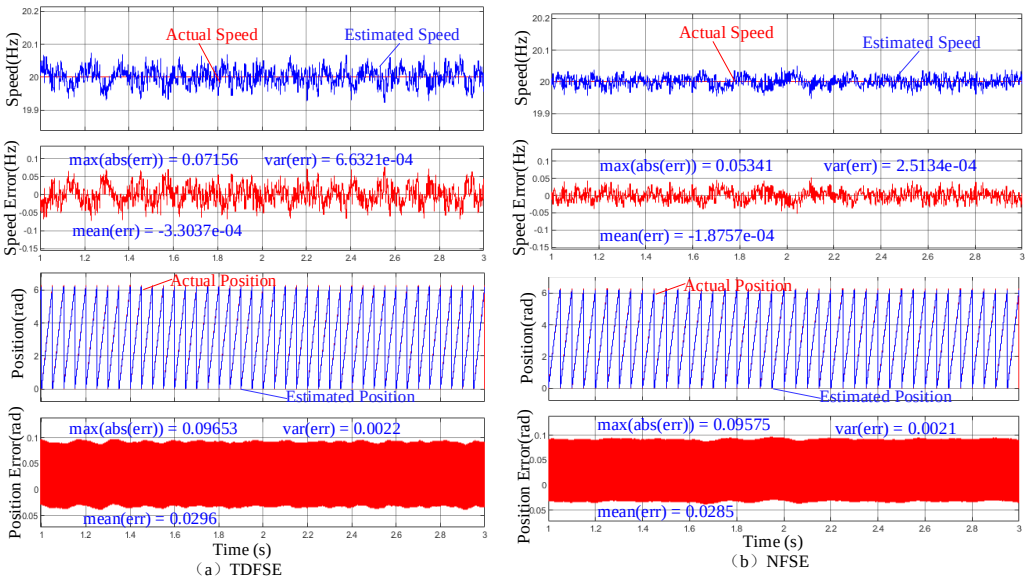

Figure 7. Steady−state simulation results at the speed of 20 Hz. (**a**) With the conventional TDFSE. (**b**) With the proposed NFSE.

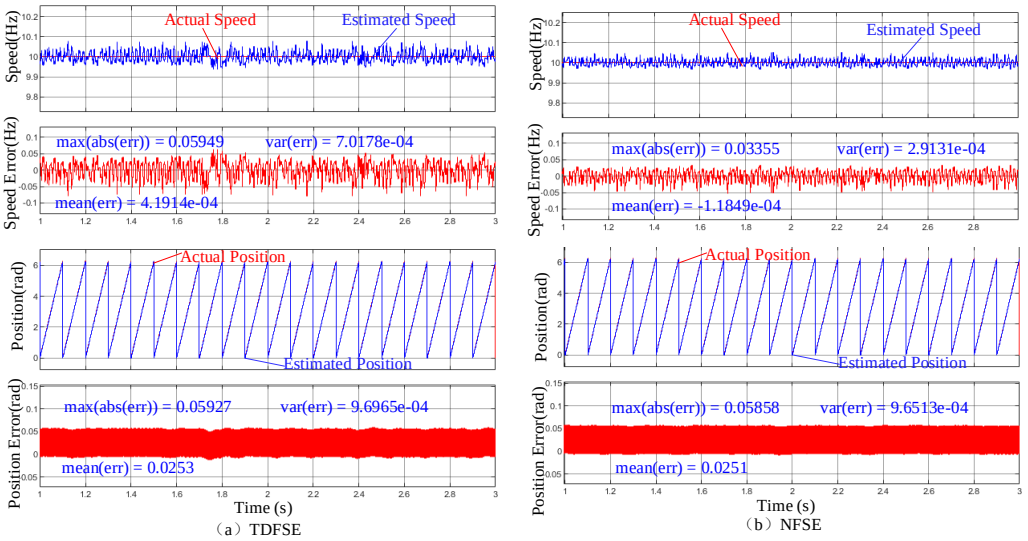

Figure 8. Steady−state simulation results at the speed of 10 Hz. (**a**) With the conventional TDFSE. (**b**) With the proposed NFSE.

In order to provide a better understanding of the simulation results, this paper has calculated the maximum absolute error (max(abs(err)), the variance of the error (var(err)), and the mean error (mean(err)) for both speed and position observations. These metrics have been annotated on the corresponding error waveform plots. Through quantitative calculations based on these metrics, it is evident that the rotor position and speed estimated using the proposed NFSE method are more accurate compared to using the conventional TDFSE method. Particularly noteworthy is the improvement in noise levels in the estimation results, especially for speed estimation. Therefore, the proposed NFSE method demonstrates better steady-state performance at lower switching-frequency applications.

Beyond steady-state performance, the dynamic performance has significance for the IPMSM drive system as well. Figure 9 illustrates the traction process of the IPMSM, ranging from 2 Hz to 20 Hz, and Figure 10 shows the braking process of the IPMSM from 20 Hz to 2 Hz.

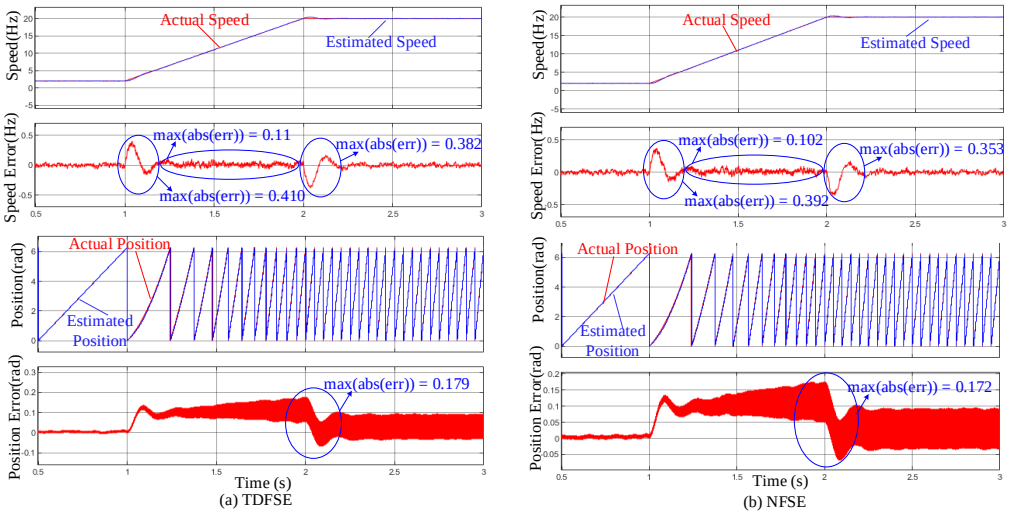

Figure 9. Simulation results of the IPMSM traction process ranging from 2 Hz to 20 Hz. (**a**) With the conventional TDFSE. (**b**) With the proposed NFSE.

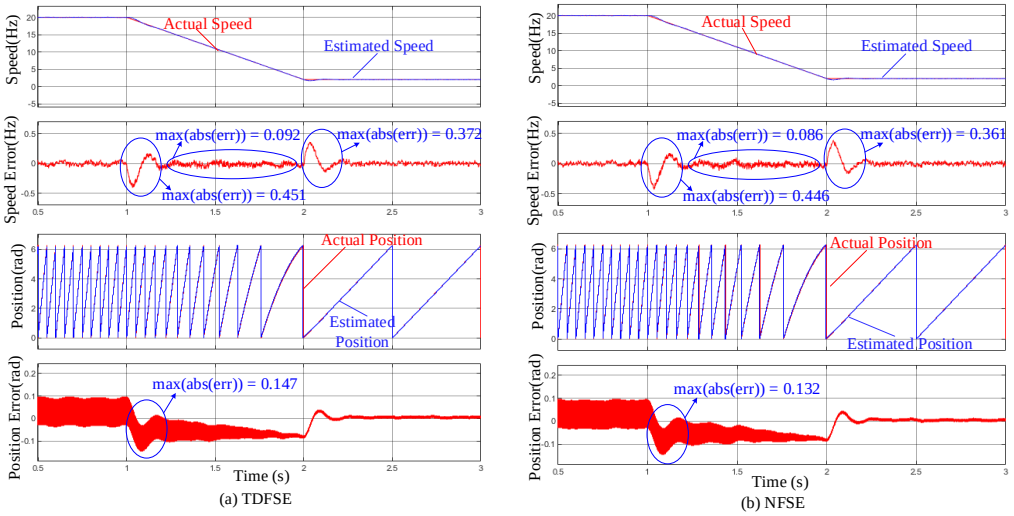

Figure 10. Simulation results of the IPMSM braking process ranging from 20 Hz to 2 Hz. (**a**) With the conventional TDFSE. (**b**) With the proposed NFSE.

For the dynamic process of traction or braking, Figures 9 and 10 show that the estimated motor speed experiences only minimal fluctuations when transitioning into or out of acceleration and deceleration states. As an intuitive comparison, the maximum absolute errors at the points of entry and exit for traction and braking, as well as during acceleration and deceleration, have been marked on the corresponding error waveform plots Compared to other methods, the conventional TDFSE approach typically demonstrates superior dynamic performance, due to its direct calculation method for signal extraction. Through quantitative comparisons, it is found that the performance of the proposed NFSE method is better than that of the conventional TDFSE method. Therefore, the proposed NFSE method also exhibits good dynamic performance in low switching-frequency applications.

In practical applications, mathematical models are affected by uncertainties and nonlinearities, leading to the generation of unwanted harmonics and noise interference in motor currents. To validate the impact of the proposed method on these harmonics and on noise interferences, this paper simulates the addition of artificial noise to the sampled three-phase motor current using a random function module in MATLAB. This simulation is designed to mimic the harmonics and noise that may be encountered in practical applications. The added three-phase noise signals are shown in Figure 11.

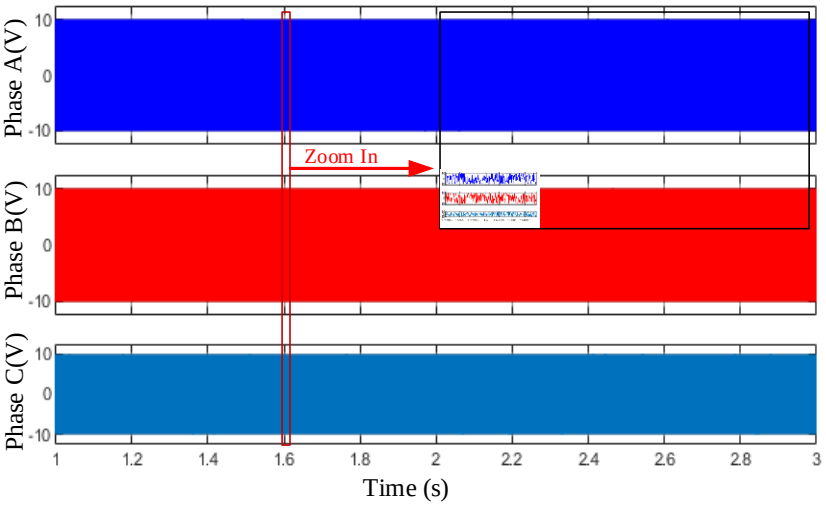

Figure 11. The artificial noise signals added to the sampled three-phase currents.

Assuming that the motor is operating at a fixed rotational speed, a simulation test is conducted with a torque of 1000 N.m applied. The results presented in Figures 12 and 13 represent the simulated test results of the traditional TDFSE and the proposed NFSE method, respectively, at 20 Hz and 10 Hz speeds after adding artificial noise to the sampled three-phase currents.

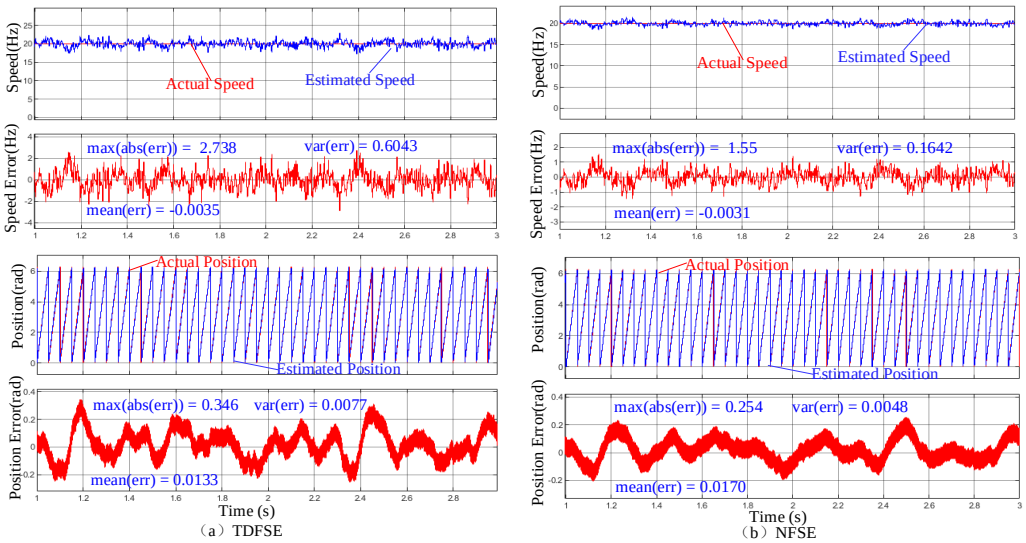

Figure 12. Simulation results at the speed of 20 Hz with artificial noise. (**a**) With the conventional TDFSE. (**b**) With the proposed NFSE.

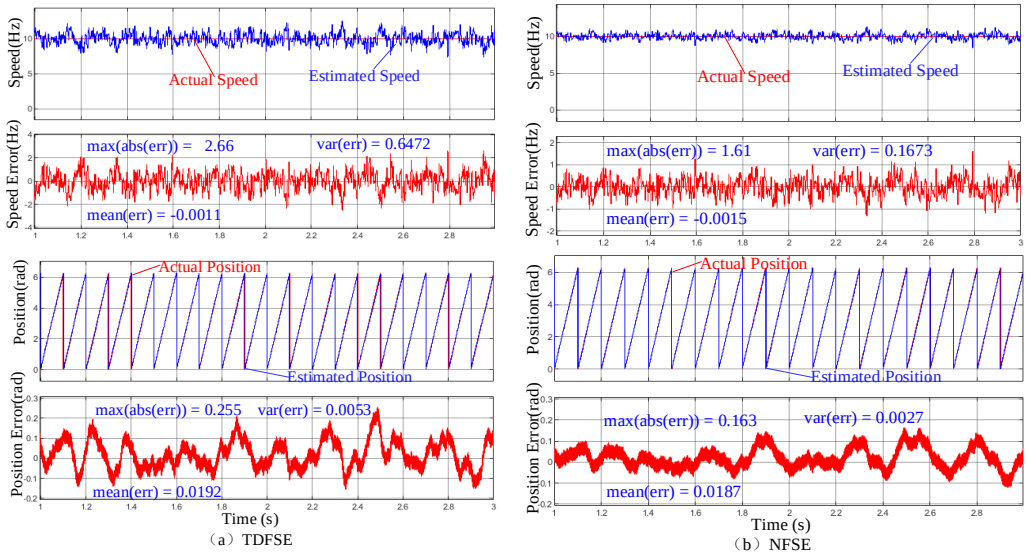

Figure 13. Simulation results at the speed of 10 Hz with artificial noise. (**a**) With the conventional TDFSE. (**b**) With the proposed NFSE.

To facilitate a comparative evaluation of the performance of the proposed NFSE method and the conventional TDFSE method under the influence of harmonics and noise, the maximum absolute error (max(abs(err)), the variance of the error (var(err)), and the mean error (mean(err)) of position and speed estimation were also calculated here, and annotations were made in the corresponding error waveform diagrams. Through a comparison, it is found that both the estimated position and speed using the proposed NFSE method were able to effectively immunize against the influence of harmonics and noise, resulting in more accurate estimation values. This demonstrates that the proposed NFSE method is more robust than traditional methods under the influence of harmonics and noise.

4.2. Experimental Validations

To further confirm the practicality of the proposed algorithm, the benchmark IPMSM drive system as outlined in Table 1 is applied in the hardware-in-the-loop (HIL) testing with the RT-LAB experimental platform illustrated in Figure 14. In the HIL testing, the models of the motor and inverter are constructed to replicate the characteristics of their real-world counterparts. By incorporating the actual motor and inverter models, including parameters like snubber resistance and capacitance of the IGBT, HIL testing can faithfully mimic real-world application scenarios. The estimated position and speed from the DSP controller (TMS320F28379D) are outputted to the RT-Lab for acquisition via a DAC chip (DAC60508). These values are then compared with the actual values, and subsequently uploaded to the main computer for further analysis.

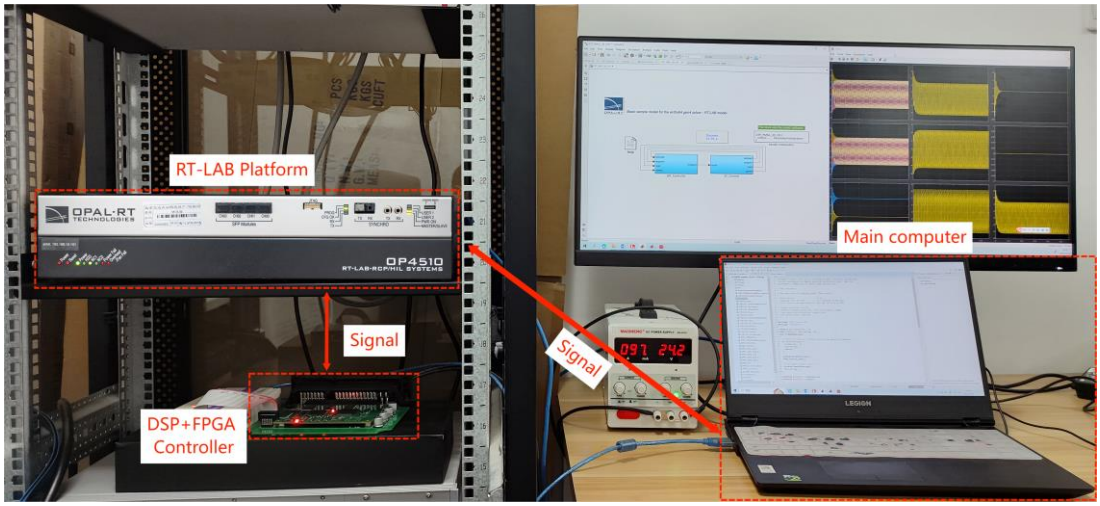

Figure 14. RT-LAB experimental platform.

The HIL testing also involves analyzing both dynamic and static aspects and comparing them with the traditional TDFSE method. The testing results depicted in Figures 15 and 16 represent the steady-state operation at speeds of 20 Hz and 10 Hz, respectively. The dynamic performance is also studied, and Figure 17 illustrates the dynamic traction and braking process.

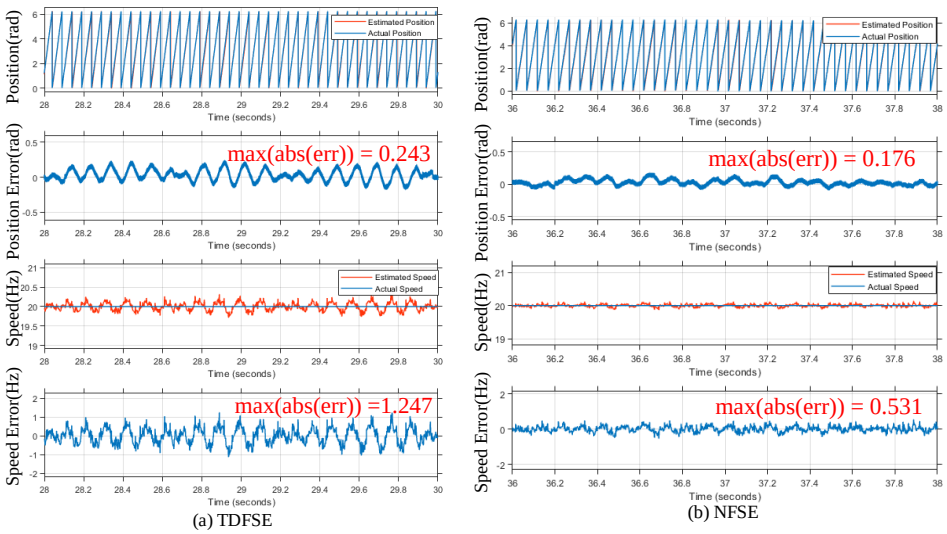

Figure 15. Steady−state HIL testing results at the speed of 20 Hz. (**a**) With the conventional TDFSE. (**b**) With the proposed NFSE.

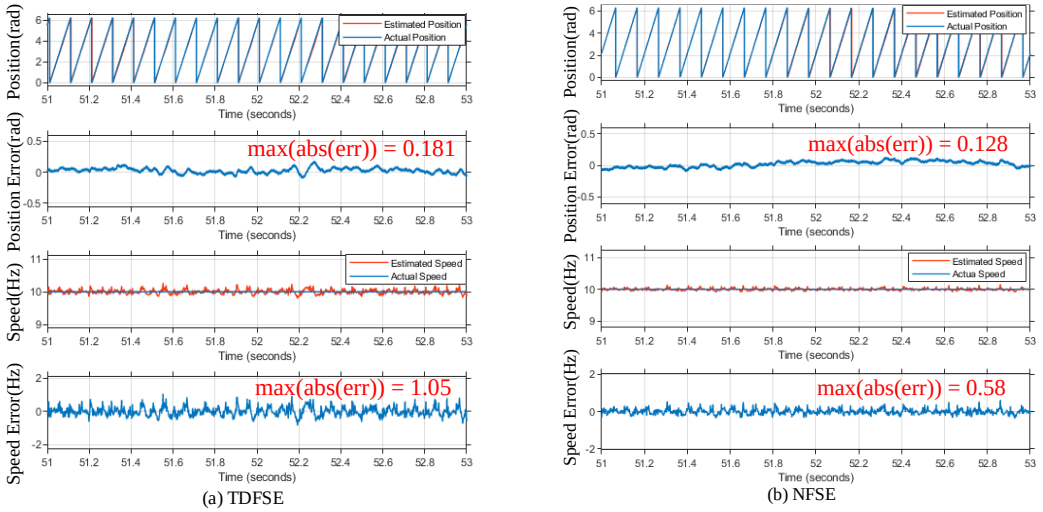

Figure 16. Steady−state HIL testing results at the speed of 10 Hz. (**a**) With the conventional TDFSE. (**b**) With the proposed NFSE.

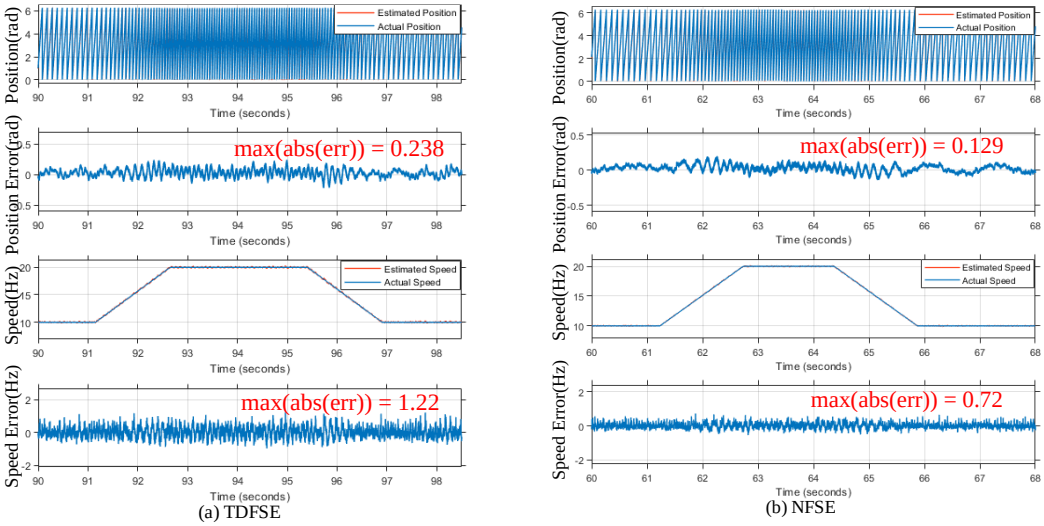

Figure 17. HIL testing results of the IPMSM traction and braking process. (**a**) With the conventional TDFSE. (**b**) With the proposed NFSE.

Analyzing the results of the HIL testing reveals that in both the static and dynamic scenarios the position and speed errors estimated by the proposed NFSE method are smaller than those of the conventional TDFSE method.

The simulation and HIL testing results above indicate that in low switching-frequency applications, the proposed NFSE method exhibits excellent performance in both static and dynamic situations. In addition, under the interference of harmonics and noise, the proposed NFSE method also demonstrated superior performance compared to traditional methods. This fully illustrates the advantage of the proposed NFSE method in applications with low switching frequencies and the presence of harmonics and noise.

5. Conclusions

To address challenges in low switching-frequency applications, this article introduces a signal-extraction method based on the NF; leveraging the advantages of the NF allows for the accurate extraction of position signals by selectively eliminating unwanted frequencies, whereas the traditional signal-extraction method based on BPF+LPF demonstrates inadequate dynamic performance, and the effectiveness of the conventional TDFSE method is limited in applications characterized by low switching frequency

and substantial noise interference. The method proposed ensures a consistent filtering performance, mitigates interference from harmonics and noise, and enhances the steady-state operating performance of the system. Simultaneously, it exhibits commendable dynamic performance, expanding the range of options for IPMSM position-sensorless control. Finally, the simulation and HIL testing outcomes have substantiated the viability and efficacy of the proposed strategy.

Author Contributions: D.M.: conceptualization, methodology, software, validation, data curation, writing—original draft. Q.W.: validation, investigation, data curation. J.Z.: validation, investigation, data curation. L.D.: conceptualization, resources, writing—review and editing. All authors have read and agreed to the published version of the manuscript.

Funding: This research received no external funding.

Institutional Review Board Statement: Not applicable.

Informed Consent Statement: Not applicable.

Data Availability Statement: All important data are included in the manuscript.

Conflicts of Interest: The authors declare no conflicts of interest.

Abbreviations

The following abbreviations are used in this manuscript:

HF	High-frequency
IPMSM	Interior permanent-magnet synchronous motor
FOC	Field-oriented control
BPF	Band-pass filter
LPF	Low-pass filter
NF	Notch filter
EMF	Electromotive force
SNR	Signal-to-noise ratio
PSVI	Pulsating sinusoidal voltage injection
PSWVI	Pulsating square-wave voltage injection
TDFSE	Time-delay filter signal extraction
NFSE	NF-based signal extraction

References

1. Song, X.; Fang, J.; Han, B.; Zheng, S. Adaptive compensation method for high-speed surface PMSM sensorless drives of EMF-based position estimation error. *IEEE Trans. Power Electron.* **2016**, *31*, 1438–1449. [CrossRef]
2. Kumar, C.D.; Shiva, B.S.; Verma, V. Vector Control of PMSM Drive with Single Current Sensor. In Proceedings of the 2020 IEEE Students Conference on Engineering & Systems (SCES), Prayagraj, India, 10–12 July 2020; pp. 1–6.
3. Zhang, G.; Wang, G.; Xu, D.; Zhao, N. ADALINE-NetworkBased PLL for Position Sensorless Interior Permanent Magnet Synchronous Motor Drives. *IEEE Trans. Power Electron.* **2016**, *31*, 1450–1460. [CrossRef]
4. Wang, G.; Yang, R.; Xu, D. DSP-Based Control of Sensorless IPMSM Drives for Wide-Speed-Range Operation. *IEEE Trans. Ind. Electron.* **2013**, *60*, 720–727. [CrossRef]
5. Gandhi, R.; Sankararao, E.; Mishra, P.; Roy, R. A Novel Technique to Correct the Unwanted Zero Position Signal of Faulty Encoder for Accurate Speed and Position Estimation of PMSM Drive. *Iran. J. Sci. Technol. Trans. Electr. Eng.* **2024**, *48*, 289–301. [CrossRef]
6. Wu, T.; Luo, D.; Wu, X.; Liu, K.; Huang, S.; Peng, X. Square-wave voltage injection based PMSM sensorless control considering time delay at low switching frequency. *IEEE Trans. Ind. Electron.* **2021**, *69*, 5525–5535. [CrossRef]
7. Wang, G.; Valla, M.; Solsona, J. Position sensorless permanent magnet synchronous machine drives—A review. *IEEE Trans. Ind. Electron.* **2019**, *67*, 5830–5842. [CrossRef]
8. Chen, Z.; Tomita, M.; Doki, S.; Okuma, S. An extended electromotive force model for sensorless control of interior permanent-magnet synchronous motors. *IEEE Trans. Ind. Electron.* **2003**, *50*, 288–295. [CrossRef]
9. Boldea, I.; Paicu, M.C.; Andreescu, G.-D. Active flux concept for motion-sensorless unified AC drives. *IEEE Trans. Power Electron.* **2008**, *23*, 2612–2618. [CrossRef]
10. Zuo, Y.; Lai, C.; Iyer, K.L. A review of sliding mode observer based sensorless control methods for PMSM drive. *IEEE Trans. Power Electron.* **2023**, *38*, 11352–11367. [CrossRef]

11. Ding, L.; Li, Y.W.; Zargari, N.R. Discrete-time SMO sensorless control of current source converter-fed PMSM drives with low switching frequency. *IEEE Trans. Ind. Electron.* **2021**, *68*, 2120–2129. [CrossRef]
12. Salman, E.; Yilmaz, M. A Novel Sensorless Control Approach for IPMSM Using Extended Flux Based PI Observer for Washing Machine Applications. *Int. J. Control. Autom. Syst.* **2023**, *21*, 2313–2322. [CrossRef]
13. Filho, C.J.V.; Vieira, R.P. Adaptive full-order observer analysis and design for sensorless interior permanent magnet synchronous motors drives. *IEEE Trans. Ind. Electron.* **2021**, *68*, 6527–6536. [CrossRef]
14. Gou, L.; Wang, C.; You, X.; Zhou, M.; Dong, S. IPMSM sensorless control for zero-and low-speed regions under low switching frequency condition based on fundamental model. *IEEE Trans. Transp. Electrif.* **2021**, *8*, 1182–1193. [CrossRef]
15. Xia, B.; Huang, S.; Zhang, J.; Zhang, W.; Liao, W.; Gao, J.; Wu, X. An Improved High-Frequency Voltage Signal Injection-based Sensorless Control of IPMSM Drives with Current Observer. *IEEE Trans. Transp. Electrif* 2023. *Early access*. [CrossRef]
16. Chen, S.; Ding, W.; Wu, X.; Huo, L.; Hu, R.; Shi, S. Sensorless control of IPMSM drives using high-frequency pulse voltage injection with random pulse sequence for audible noise reduction. *IEEE Trans. Power Electron.* **2023**, *38*, 9395–9408. [CrossRef]
17. Basic, D.; Malrait, F.; Rouchon, P. Current controller forlow-frequency signal injection and rotor flux position tracking at low speeds. *IEEE Trans. Ind. Electron.* **2011**, *58*, 4010–4022. [CrossRef]
18. Mai, Z.; Xiao, F.; Fu, K.; Liu, J.; Lian, C.; Li, K.; Zhang, W. HF pulsating carrier voltage injection method based on improved position error signal extraction strategy for PMSM position sensorless control. *IEEE Trans. Power Electron.* **2021**, *36*, 9348–9360. [CrossRef]
19. Corley, M.J.; Lorenz, R.D. Rotor position and velocity estimation for a salient-pole permanent magnet synchronous machine at standstill and high speeds. *IEEE Trans. Ind. Appl.* **1998**, *34*, 784–789. [CrossRef]
20. Linke, M.; Kennel, R.; Holtz, J. Sensorless speed and position control of synchronous machines using alternating carrier injection. In Proceedings of the IEEE International Electric Machines and Drives Conference (IEMDC'03), Madison, WI, USA, 1–4 June 2003; Volume 2, pp. 1211–1217.
21. Naderian, M.; Markadeh, G.A.; Karimi-Ghartemani, M.; Mojiri, M. Improved sensorless control strategy for IPMSM using an ePLL approach with high-frequency injection. *IEEE Trans. Ind. Electron.* **2023**, *71*, 2231–2241. [CrossRef]
22. Zhang, G.; Wang, G.; Wang, H.; Xiao, D.; Li, L.; Xu, D.G. Pseudo-Random-Frequency Sinusoidal Injection Based Sensorless IPMSM Drives with Tolerance for System Delays. *IEEE Trans. Powe Electron.* **2019**, *34*, 3623–3632. [CrossRef]
23. Zhang, P.; Wang, S.; Li, Y. A Novel Dual Random Scheme in Signal Injection Sensorless Control of IPMSM Drives for High-Frequency Harmonics Reduction. *IEEE Trans. Power Electron.* **2023**, *99*, 1–13. [CrossRef]
24. Wang, G.; Zhou, H.; Zhao, N.; Li, C.; Xu, D. Sensorless control of IPMSM drives using a pseudo-random phase-switching fixed-frequency signal injection scheme. *IEEE Trans. Ind. Electron.* **2018**, *65*, 7660–7671. [CrossRef]
25. Szalai, T.; Berger, G.; Petzoldt, J. Stabilizing sensorless control down to zero speed by using the high-frequency current amplitude. *IEEE Trans. Power Electron.* **2014**, *29*, 3646–3656. [CrossRef]
26. Reigosa, D.D.; Briz, F.; Blanco, C.; Guerrero, J.M. Sensorlesscontrol of doubly-fed induction generators based on stator high frequency signal injection. *IEEE Trans. Ind. Appl.* **2014**, *50*, 3382–3391. [CrossRef]
27. Li, H.; Zhang, X.; Yang, S.; Liu, S. Unified graphical model of highfrequency signal injection methods for PMSM sensorless control. *IEEE Trans. Ind. Electron.* **2020**, *67*, 4411–4421. [CrossRef]
28. Gong, L.; Zhu, Z. Robust initial rotor position estimation of permanentmagnet brushless AC machines with carrier-signal-injection-based sensorless control. *IEEE Trans. Ind. Appl.* **2013**, *49*, 2602–2609. [CrossRef]
29. Yoon, Y.; Sul, S.; Morimoto, S.; Ide, K. High-bandwidth sensorless algorithm for ac machines based on square-wave-type voltage injection. *IEEE Trans. Ind. Appl.* **2011**, *47*, 1361–1370. [CrossRef]
30. Tang, Q.; Shen, A.; Luo, X.; Xu, J. PMSM sensorless control by injecting HF pulsating carrier signal into ABC frame. *IEEE Trans. Power Electron.* **2017**, *32*, 3767–3776. [CrossRef]
31. Luo, X.; Tang, Q.; Shen, A.; Zhang, Q. PMSM sensorless control by injecting HF pulsating carrier signal into estimated fixed-frequency rotating reference frame. *IEEE Trans. Ind. Electron.* **2016**, *63*, 2294–2303. [CrossRef]
32. Zhang, G.; Wang, G.; Yuan, B.; Liu, R.; Xu, D. Active disturbance rejection control strategy for signal injection-based sensorless IPMSM drives. *IEEE Trans. Transp. Electrif.* **2017**, *4*, 330–339. [CrossRef]
33. Karimi-Ghartemani, M.; Khajehoddin, S.A.; Jain, P.K.; Bakhshai, A.; Mojiri, M. Addressing DC component in PLL and notch filter algorithms. *IEEE Trans. Power Electron.* **2011**, *27*, 78–86. [CrossRef]
34. Ge, Y.; Yang, L.; Ma, X. A harmonic compensation method for SPMSM sensorless control based on the orthogonal master-slave adaptive notch filter. *IEEE Trans. Power Electron.* **2021**, *36*, 11701–11711. [CrossRef]
35. Zhang, G.; Wang, G.; Ni, R.; Xu, D. Adaptive notch filter based harmonic self-compensated sliding-mode observer for position sensorless IPMSM drives. In Proceedings of the 2015 9th International Conference on Power Electronics and ECCE Asia (ICPE-ECCE Asia), Seoul, Republic of Korea, 1–5 June 2015; pp. 1123–1128.
36. Wang, Y.; Xue, Z.; Luo, G.; Chen, Z. A Time-Delay Compensation Method for PMSM Sensorless Control System under Low Switching Frequency. In Proceedings of the IECON 2019—45th Annual Conference of the IEEE Industrial Electronics Society, Lisbon, Portugal, 14–17 October 2019; pp. 880–885.

37. Guo, B.-Y.; Pei, S.-C.; Lu, W.-Y. Pole-zero assignment of all-pass-based notch filters. *IEEE Trans. Circuits Syst. II Express Briefs* **2017**, *64*, 477–481.
38. Sharma, A.; Rawat, T.K.; Agrawal, A. Design and FPGA implementation of lattice wave digital notch filter with minimal transient duration. *IET Signal Process.* **2020**, *14*, 440–447. [CrossRef]